AIMS Mathematics

https://www.aimspress.com/journal/Math

AIMS Mathematics, 11(9): 30233–30259.
DOI: 10.3934/math.20261198
Received: 28 June 2026
Revised: 26 August 2026
Accepted: 31 August 2026
Published: 17 September 2026

Research article

Mean-square stability and semi-implicit Euler-Maruyama approximation of a stochastic pantograph heat equation with proportional space-time delay

Fathalla A. Rihan*

Department of Mathematical Sciences, College of Science, United Arab Emirates University, Al-Ain, 15551, United Arab Emirates

* **Correspondence:** Email: frihan@uaeu.ac.ae.

Abstract: We studied a stochastic heat equation with proportional space-time delay and scalar multiplicative Brownian noise. The model described diffusion with scale-dependent memory, where delayed feedback was evaluated at spatially rescaled locations. A key feature was that the associated spatial pantograph operator is non-isometric, leading to an additional spatial-compression effect in the mean-square stability condition. We established well-posedness, mean-square boundedness, and algebraic mean-square decay under suitable stability assumptions. For the numerical approximation, we developed a semi-implicit finite-difference Euler-Maruyama method that treated diffusion and damping implicitly while evaluating the delayed and stochastic terms explicitly. Under appropriate interpolation and step-size assumptions, the scheme preserved mean-square boundedness and algebraic decay and achieved second-order spatial accuracy and the classical one-half strong temporal order. Numerical experiments supported the theoretical results, demonstrated the effectiveness of the semi-implicit treatment of stiffness, and quantified the influence of spatial compression on the stability margin.

Keywords: stochastic heat equation; space-time pantograph delay; mean-square stability; semi-implicit Euler-Maruyama method; strong convergence
Mathematics Subject Classification: 34K05, 34K50, 60H15, 65C30, 65M06

1. Introduction

Delay effects arise when the evolution of a system depends on earlier states. In contrast to classical delay equations with a fixed lag, pantograph equations involve proportional arguments and are therefore well suited to describing scale-dependent memory [1–3]. In spatially distributed problems, this idea leads naturally to feedback evaluated at both an earlier time and a rescaled spatial location. Deterministic pantograph diffusion models and numerical schemes have been investigated in [4–6].

Stochastic pantograph differential equations, including convergence and mean-square stability, have been considered in [7]. Related developments for fractional pantograph systems, functional inclusions with delay, and mixed-delay equations can be found in [8–10]. Related numerical studies of nonlinear and nonclassical heat-transfer models include [11, 12]. Although these latter studies are deterministic and do not involve stochastic pantograph terms, they provide useful computational context for parameter-sensitive diffusion problems.

The combined treatment of parabolic diffusion, proportional space-time memory, and stochastic forcing is comparatively less developed. The model considered here is intended as a prototype in which these mechanisms can be separated and analyzed explicitly. Spatial diffusion is represented by the Laplacian, local dissipation by a damping term, memory by feedback sampled at a proportional past time and a compressed spatial location, and environmental uncertainty by scalar multiplicative Brownian noise. This structure is simple enough to permit a transparent stability analysis while retaining the essential features of a diffusion system with scale-dependent memory.

We study the stochastic heat equation

$$du(x,t) = [u_{xx}(x,t) - \mu u(x,t) + \nu u(\eta x, \lambda t)]\,dt + \sigma u(x,t)\,dW(t), \quad (x,t) \in (0,L) \times (0,T], \tag{1.1}$$

where $\mu > 0$ is the damping coefficient, $\nu \geq 0$ is the delayed-feedback strength, $\sigma \geq 0$ is the multiplicative-noise intensity, and $0 < \eta, \lambda < 1$. The parameter λ determines the proportional temporal memory, whereas η determines the spatial compression. The scalar Brownian motion $W(t)$ acts coherently across the spatial domain, so (1.1) is an infinite-dimensional stochastic evolution equation driven by scalar noise rather than by space-time white noise. The boundary and initial data completing the problem are specified at the beginning of Section 2.

A distinctive feature of (1.1) is the spatial pantograph operator, which evaluates the state at a compressed spatial location. This spatial rescaling is non-isometric in $L^2(0, L)$ and therefore changes the energy norm. The resulting compression factor is quantified in Lemma 2.1 and introduces an additional dependence on the spatial-scaling parameter in the mean-square stability threshold. In the absence of spatial rescaling, the model reduces to a proportional time-delay problem. Figure 1 illustrates the simultaneous proportional scaling in space and time.

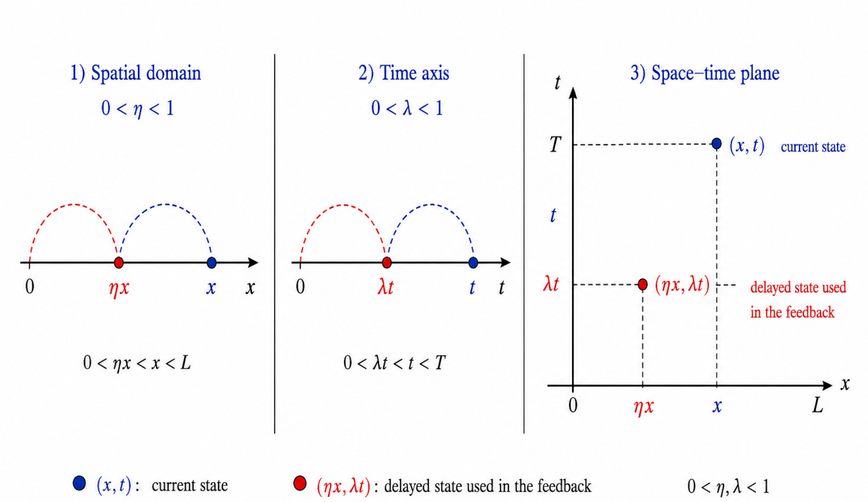

Figure 1. Schematic of the proportional space-time delay $u(\eta x, \lambda t)$. The delayed feedback is evaluated at the compressed spatial point ηx and the proportional past time λt.

The major contributions are as follows.

- We formulate (1.1) as a Hilbert-space stochastic evolution equation and establish well-posedness, mean-square boundedness, and algebraic mean-square decay. The analysis identifies the effect of the spatial pantograph operator on the stability threshold.
- We develop a semi-implicit finite-difference Euler-Maruyama method with implicit diffusion and damping and explicit delay and noise. Under suitable conditions, the scheme preserves mean-square stability and algebraic decay and achieves second-order spatial and one-half temporal strong convergence.
- Numerical experiments support the analysis by examining delay interpolation, stiffness control, convergence, and sensitivity to the spatial-scaling parameter η.

The remainder of this paper is organized as follows. Section 2 presents the well-posedness and mean-square stability analysis. Section 3 develops and analyzes the semi-implicit Euler-Maruyama scheme. Section 4 reports the numerical experiments. Finally, Section 5 gives the conclusions. The basic implementation of the semi-implicit Euler-Maruyama method is summarized in Algorithm 1.

Algorithm 1 Semi-implicit Euler-Maruyama algorithm

```
Choose L, M, Δx = L/M, T, Δt, and set N = ⌊T/Δt⌋.
Define x_i = iΔx, t_n = nΔt, construct A_h, and set B_h = I − Δt(A_h − μI).
Set U^0 from φ(·, 0) and impose homogeneous boundary values.
for n = 0, 1, ..., N − 1 do
    Generate ΔW_n = √Δt ξ_n, ξ_n ~ N(0, 1), and set t_d = λt_n.
    If t_d = 0, set Ũ^n = U^0. Otherwise, find k ≤ n − 1 such that t_k ≤ t_d ≤ t_{k+1} ≤ t_n, set θ = (t_d − t_k)/Δt,
    and compute Ũ^n = (1 − θ)U^k + θU^{k+1}.
    Impose Ũ^n_0 = Ũ^n_M = 0.
    for i = 1, ..., M − 1 do
        Set x^η_i = ηx_i, choose j with x_j ≤ x^η_i ≤ x_{j+1}, and set ρ_i = (x^η_i − x_j)/Δx.
        Compute Û^n_{η,i} = (1 − ρ_i)Ũ^n_j + ρ_i Ũ^n_{j+1}.
    end for
    Set R^n = U^n + Δt νÛ^n_η + σU^n ΔW_n.
    Solve B_h U^{n+1} = R^n and impose homogeneous boundary values.
end for
```

2. Well-posedness and mean-square stability

This section develops the analytical framework for the stochastic pantograph heat equation. We first formulate the problem in a Hilbert-space setting and establish well-posedness, and then derive conditions for mean-square boundedness and algebraic mean-square decay.

Let $D = (0, L)$ and $H = L^2(D; \mathbb{R})$. The stochastic equation (1.1) is supplemented by the homogeneous Dirichlet boundary conditions

$$u(0, t) = u(L, t) = 0, \qquad t \geq 0, \tag{2.1}$$

and the initial history

$$u(x,t) = \phi(x,t), \qquad x \in D, \quad t \le 0. \tag{2.2}$$

Here, $W(t)$ is a standard one-dimensional Brownian motion on a filtered probability space $(\Omega, \mathcal{F}, \{\mathcal{F}_t\}_{t\ge 0}, \mathbb{P})$ satisfying the usual conditions. The parameter ranges are $\mu > 0$, $\nu \ge 0$, $\sigma \ge 0$, and $0 < \eta, \lambda < 1$. Throughout this section, C denotes a positive constant, independent of the solution, whose value may change from line to line.

Assumption 2.1. *For every $t \le 0$, the history satisfies $\phi(\cdot, t) \in L^2(\Omega; H_0^1(D))$, with*

$$\sup_{t\le 0} \mathbb{E}\|\phi(\cdot,t)\|^2_{L^2(D)} < \infty.$$

Moreover, $t \mapsto \phi(\cdot, t)$ is continuous as a map into $L^2(\Omega; L^2(D))$, and $\phi(\cdot, 0)$ is $\mathcal{F}_0$-measurable.

Remark 2.1. *Since $0 < \lambda < 1$, we have $\lambda t \in [0, t]$ for every $t \ge 0$. Thus, the delayed argument never enters negative times, and only $\phi(\cdot, 0)$ is needed to evolve the present proportional-delay problem forward from $t = 0$. The history formulation in (2.2) is retained for consistency with the standard framework of stochastic functional differential equations [13] and to facilitate extensions to fixed or distributed delays.*

Remark 2.2. *The analysis is stated for $\nu \ge 0$, corresponding to positive delayed feedback. If $\nu < 0$, the delayed term may provide additional damping; the estimates below remain valid after replacing ν by $|\nu|$.*

2.1. Hilbert-space formulation

Equip $H = L^2(D; \mathbb{R})$ with the inner product and norm

$$\langle u, v\rangle_H = \int_0^L u(x)v(x)\,dx, \quad \|u\|_H^2 = \int_0^L |u(x)|^2\,dx. \tag{2.3}$$

For brevity, the subscript H will be omitted whenever no ambiguity can arise. Define the Dirichlet Laplacian

$$Au = u_{xx}, \quad D(A) = H^2(D) \cap H_0^1(D). \tag{2.4}$$

Then, A is self-adjoint and negative definite, and

$$\langle Au, u\rangle = -\|u_x\|^2, \quad u \in D(A).$$

The first Dirichlet eigenvalue of $-A$ is $\kappa_1 = (\pi/L)^2$. Hence, Poincaré's inequality gives

$$\|u_x\|^2 \ge \kappa_1 \|u\|^2, \quad u \in H_0^1(D). \tag{2.5}$$

The spatial rescaling in (1.1) is represented by the pantograph operator

$$(Pv)(x) = v(\eta x), \quad x \in D. \tag{2.6}$$

Lemma 2.1. *(Boundedness of the spatial pantograph operator) For every $v \in H$,*

$$\|Pv\|^2 \le \frac{1}{\eta}\|v\|^2. \tag{2.7}$$

Consequently, $P \in \mathcal{L}(H)$ and $\|P\|_{\mathcal{L}(H)} \le \eta^{-1/2}$.

Proof. Set $z = \eta x$. Then, $dx = dz/\eta$, and the interval $[0, L]$ is mapped onto $[0, \eta L]$. Therefore,

$$\|Pv\|^2 = \int_0^L |v(\eta x)|^2 \, dx = \frac{1}{\eta} \int_0^{\eta L} |v(z)|^2 \, dz \le \frac{1}{\eta} \int_0^L |v(z)|^2 \, dz = \frac{1}{\eta} \|v\|^2. \tag{2.8}$$

The inequality follows from $0 < \eta < 1$, which implies $[0, \eta L] \subset [0, L]$, together with the nonnegativity of $|v(z)|^2$. This calculation also explains the appearance of the factor η^{-1} in the squared L^2 estimate.

Remark 2.3. *The operator P is used only as a bounded operator on H; it is not required to preserve the Dirichlet domain $D(A)$.*

Remark 2.4. *(Multidimensional extension) If $D \subset \mathbb{R}^d$ and $\eta D \subset D$, the same change of variables gives, for $(P_\eta v)(x) = v(\eta x)$,*

$$\|P_\eta v\|^2_{L^2(D)} = \eta^{-d} \int_{\eta D} |v(z)|^2 \, dz \le \eta^{-d} \|v\|^2_{L^2(D)}.$$

Thus, the one-dimensional factor η^{-1} is replaced by η^{-d}. A full multidimensional analysis would additionally depend on the geometry of D, the first Dirichlet eigenvalue of $-\Delta$, and the corresponding interpolation estimates; we therefore restrict the present paper to $D = (0, L)$.

Using (2.4) and (2.6), model (1.1) is equivalently written as the H-valued stochastic evolution equation

$$du(t) = \left[Au(t) - \mu u(t) + \nu P u(\lambda t)\right] dt + \sigma u(t) \, dW(t). \tag{2.9}$$

Definition 2.1. *(Mild solution) Let $S(t) = e^{tA}$ be the heat semigroup generated by A. An adapted H-valued process u is a mild solution of* (2.9) *on $[0, T]$ if $u \in L^2(\Omega; C([0, T]; H))$, $u(0) = \phi(\cdot, 0)$ almost surely, and, for every $t \in [0, T]$,*

$$u(t) = S(t)\phi(\cdot, 0) + \int_0^t S(t - s)[-\mu u(s) + \nu P u(\lambda s)] ds + \int_0^t S(t - s)\sigma u(s) \, dW(s) \tag{2.10}$$

almost surely.

Theorem 2.1. *(Well-posedness) Assume Assumption 2.1. Then, for every $T > 0$,* (2.9) *admits a unique mild solution*

$$u \in L^2(\Omega; C([0, T]; H)).$$

Moreover, there exists a constant $C_T > 0$, depending on T, μ, ν, σ, and η, but not on the solution, such that

$$\mathbb{E} \sup_{0 \le t \le T} \|u(t)\|^2 \le C_T \left(1 + \mathbb{E}\|\phi(\cdot, 0)\|^2\right). \tag{2.11}$$

Proof. The Dirichlet Laplacian A generates a contractive analytic semigroup on H; standard semigroup theory for stochastic evolution equations provides the underlying framework [14, 15]. The maps $u \mapsto -\mu u$ and $u \mapsto \sigma u$ are globally Lipschitz on H, while Lemma 2.1 shows that P is bounded. Moreover, if v is adapted, then $Pv(\lambda s)$ is $\mathcal{F}_s$-measurable because $\lambda s \le s$.

Define Φ by the righthand side of (2.10). The semigroup contraction property, the boundedness of P, and the Burkholder-Davis-Gundy inequality give, for two adapted processes u and v,

$$\mathbb{E} \sup_{0 \le r \le t} \|\Phi u(r) - \Phi v(r)\|^2 \le C \int_0^t \mathbb{E} \sup_{0 \le q \le s} \|u(q) - v(q)\|^2 \, ds.$$

A standard Picard iteration on sufficiently short intervals, followed by continuation, yields existence and uniqueness. Applying the corresponding a priori estimate to the fixed point and then Gronwall's inequality gives (2.11). Since $T > 0$ is arbitrary and the coefficients are globally Lipschitz, the solution extends uniquely to every finite time interval.

Remark 2.5. *The operator estimate in Lemma 2.1 gives $\|P\| \le \eta^{-1/2}$, whereas the squared estimate* (2.7) *introduces the factor η^{-1} into the second-moment energy inequality. Consequently, stronger spatial compression (smaller η) weakens the sufficient stability margin.*

2.2. Mean-square stability and algebraic decay

Set

$$Y(t) := \mathbb{E}\|u(t)\|^2.$$

Applying Itô's formula to $V(u) = \|u\|^2$, using the standard stochastic-calculus framework [16], first for sufficiently regular solutions and then by a standard approximation argument for mild solutions, yields

$$d\|u(t)\|^2 = 2\langle u(t), Au(t) - \mu u(t) + \nu Pu(\lambda t)\rangle\,dt + \sigma^2\|u(t)\|^2\,dt + 2\sigma\|u(t)\|^2\,dW(t). \tag{2.12}$$

The stochastic integral in (2.12) has zero expectation because its integrand is adapted and square integrable, while the quadratic-variation contribution is $\sigma^2\|u(t)\|^2dt$. Taking expectations therefore gives

$$\frac{d}{dt}\mathbb{E}\|u(t)\|^2 = 2\mathbb{E}\langle u(t), Au(t)\rangle - 2\mu\mathbb{E}\|u(t)\|^2 + 2\nu\mathbb{E}\langle u(t), Pu(\lambda t)\rangle + \sigma^2\mathbb{E}\|u(t)\|^2. \tag{2.13}$$

Since $\langle Au, u\rangle = -\|u_x\|^2$,

$$\frac{d}{dt}\mathbb{E}\|u(t)\|^2 = -2\mathbb{E}\|u_x(t)\|^2 - (2\mu - \sigma^2)\mathbb{E}\|u(t)\|^2 + 2\nu\mathbb{E}\langle u(t), Pu(\lambda t)\rangle. \tag{2.14}$$

By Young's inequality and Lemma 2.1,

$$2\nu\langle u(t), Pu(\lambda t)\rangle \le \nu\|u(t)\|^2 + \nu\|Pu(\lambda t)\|^2 \le \nu\|u(t)\|^2 + \frac{\nu}{\eta}\|u(\lambda t)\|^2. \tag{2.15}$$

Consequently,

$$\frac{d}{dt}\mathbb{E}\|u(t)\|^2 \le -2\mathbb{E}\|u_x(t)\|^2 - (2\mu - \sigma^2 - \nu)\mathbb{E}\|u(t)\|^2 + \frac{\nu}{\eta}\mathbb{E}\|u(\lambda t)\|^2. \tag{2.16}$$

Using Poincaré's inequality (2.5), we arrive at the scalar pantograph inequality

$$Y'(t) \le -\alpha Y(t) + \beta Y(\lambda t), \tag{2.17}$$

where

$$\alpha = 2\kappa_1 + 2\mu - \sigma^2 - \nu, \quad \beta = \frac{\nu}{\eta}. \tag{2.18}$$

Proposition 2.1. *(Weighted stability condition) For any $\vartheta > 0$,*

$$2\nu\langle u(t), Pu(\lambda t)\rangle \le \nu\vartheta\|u(t)\|^2 + \frac{\nu}{\vartheta\eta}\|u(\lambda t)\|^2. \tag{2.19}$$

Hence,

$$Y'(t) \le -\alpha_\vartheta Y(t) + \beta_\vartheta Y(\lambda t), \quad \alpha_\vartheta = 2\kappa_1 + 2\mu - \sigma^2 - \nu\vartheta, \quad \beta_\vartheta = \frac{\nu}{\vartheta\eta}. \tag{2.20}$$

If $\alpha_\vartheta > \beta_\vartheta$ for some $\vartheta > 0$, the comparison argument below gives mean-square boundedness and algebraic decay. Optimizing the balance $\nu\vartheta + \nu/(\vartheta\eta)$ over $\vartheta > 0$ gives $\vartheta = \eta^{-1/2}$ and the sufficient condition

$$2\left(\frac{\pi}{L}\right)^2 + 2\mu - \sigma^2 > \frac{2\nu}{\sqrt{\eta}}. \tag{2.21}$$

Since $2/\sqrt{\eta} \le 1 + 1/\eta$ for $0 < \eta < 1$, (2.21) *is less conservative than* (2.23) *below.*

Theorem 2.2. *(Mean-square boundedness) Assume*

$$\alpha > \beta. \tag{2.22}$$

Equivalently,

$$2\left(\frac{\pi}{L}\right)^2 + 2\mu > \sigma^2 + \nu\left(1 + \frac{1}{\eta}\right). \tag{2.23}$$

Then, the mild solution of (2.9) *is uniformly mean-square bounded. In particular, with*

$$M_0 := \mathbb{E}\|\phi(\cdot, 0)\|^2,$$

one has

$$\mathbb{E}\|u(t)\|^2 \le M_0, \quad t \ge 0.$$

Proof. From (2.17),

$$Y'(t) \le -\alpha Y(t) + \beta Y(\lambda t), \quad t \ge 0,$$

and $Y(0) = M_0$. Suppose that Y crosses the level $M_0 + \varepsilon$ for some $\varepsilon > 0$, and let $t_* > 0$ be the first crossing time. Then,

$$Y(t_*) = M_0 + \varepsilon, \quad Y(s) < M_0 + \varepsilon \quad (0 \le s < t_*).$$

Since $0 < \lambda < 1$, we have $\lambda t_* < t_*$ and therefore $Y(\lambda t_*) \le Y(t_*)$. Hence,

$$D^+Y(t_*) \le -\alpha Y(t_*) + \beta Y(\lambda t_*) \le -(\alpha - \beta)Y(t_*) < 0,$$

which contradicts an upward crossing. Thus, $Y(t) \le M_0$ for every $t \ge 0$.

Theorem 2.3. *(Algebraic mean-square decay) Assume* (2.22). *If $\beta > 0$, choose $q > 0$ such that*

$$\beta\lambda^{-q} < \alpha, \quad \textit{equivalently} \quad 0 < q < \frac{\log(\alpha/\beta)}{\log(1/\lambda)}. \tag{2.24}$$

If $\beta = 0$, any fixed $q > 0$ is admissible. Then, there exists $C_q > 0$ such that

$$\mathbb{E}\|u(t)\|^2 \le C_q(1 + t)^{-q}, \quad t \ge 0. \tag{2.25}$$

Consequently, the zero solution is mean-square asymptotically stable.

Proof. Let $Y(t) = \mathbb{E}\|u(t)\|^2$. Choose q as stated and then choose $a \geq 1$ sufficiently large that

$$\alpha - \beta\lambda^{-q} - \frac{q}{a} > 0.$$

Set

$$Z(t) = K(a + t)^{-q},$$

where $K > 0$ is chosen so that $Z(0) \geq Y(0)$. Since

$$\frac{Z(\lambda t)}{Z(t)} = \left(\frac{a + t}{a + \lambda t}\right)^q \leq \lambda^{-q}, \quad -\frac{Z'(t)}{Z(t)} = \frac{q}{a + t} \leq \frac{q}{a},$$

we have

$$Z'(t) + \alpha Z(t) - \beta Z(\lambda t) \geq Z(t)\left(\alpha - \beta\lambda^{-q} - \frac{q}{a}\right) > 0.$$

If $Y - Z$ had a first positive contact at $t_* > 0$, then $Y(t_*) = Z(t_*)$ and, because $\lambda t_* < t_*$, also $Y(\lambda t_*) \leq Z(\lambda t_*)$. Therefore,

$$D^+(Y - Z)(t_*) \leq -\alpha Z(t_*) + \beta Z(\lambda t_*) - Z'(t_*) < 0,$$

contradicting upward crossing. Hence, $Y(t) \leq Z(t)$ for all $t \geq 0$. Since $(a + t)^{-q} \leq C(1 + t)^{-q}$, (2.25) follows.

Corollary 2.1. *(Conservative boundedness condition) A simpler sufficient condition, obtained by dropping the stabilizing diffusion contribution from* (2.23)*, is*

$$2\mu > \sigma^2 + \nu\left(1 + \frac{1}{\eta}\right).$$

It is more restrictive than (2.23)*, but can be useful for a quick parameter check.*

Corollary 2.2. *(No spatial rescaling) If $\eta = 1$, then P is the identity in the spatial variable and* (2.23) *reduces to*

$$2\left(\frac{\pi}{L}\right)^2 + 2\mu > \sigma^2 + 2\nu.$$

Thus, the additional penalty in the present model is induced by the spatial compression $x \mapsto \eta x$.

Remark 2.6. *Condition* (2.23) *displays the stability balance directly: Diffusion and damping are stabilizing, whereas multiplicative noise and delayed feedback are destabilizing. In particular, the sufficient stability margin increases with stronger damping and weaker noise or feedback, and decreases as η becomes smaller.*

3. Semi-implicit Euler-Maruyama: discretization and analysis

In this section, we develop a semi-implicit finite-difference Euler-Maruyama method for the stochastic pantograph heat equation. Diffusion and damping are treated implicitly, while the proportional delay and stochastic terms are evaluated explicitly to control the stiffness induced by the discrete Laplacian.

This splitting damps high-frequency spatial modes through $A_h - \mu I$, uses only previously computed values for the delayed term since $\lambda t_n \leq t_n$, and reflects the stability balance of the continuous problem: diffusion and damping are stabilizing, whereas noise and delayed feedback are destabilizing.

The spatial discretization, reconstruction of the proportional delay, and fully discrete stochastic update are introduced successively below. Throughout this section, $h := \Delta x$ denotes the spatial mesh parameter; subscripts h indicate mesh-dependent quantities.

3.1. Spatial semi-discretization

Let $0 = x_0 < x_1 < \cdots < x_M = L$, $\Delta x = \frac{L}{M}$, $x_i = i\Delta x$. We denote by $U_i(t)$ an approximation of $u(x_i, t)$, for $i = 1, \ldots, M-1$, and impose the homogeneous boundary conditions by setting

$$U_0(t) = U_M(t) = 0.$$

The second derivative is approximated by the standard central difference formula

$$u_{xx}(x_i, t) \approx \frac{U_{i+1}(t) - 2U_i(t) + U_{i-1}(t)}{(\Delta x)^2}, \quad i = 1, \ldots, M-1. \tag{3.1}$$

Writing

$$U(t) = (U_1(t), U_2(t), \ldots, U_{M-1}(t))^T, \tag{3.2}$$

and applying (3.1) at each interior node gives one row with coefficients $1, -2, 1$. Collecting these $M-1$ nodal equations and using $U_0 = U_M = 0$ yields the tridiagonal discrete Dirichlet Laplacian below. Thus, A_h is obtained directly from the central-difference stencil, not introduced independently. We obtain the semi-discrete system

$$dU(t) = \left[A_h U(t) - \mu U(t) + \nu U_\eta(\lambda t)\right] dt + \sigma U(t) dW(t), \tag{3.3}$$

where

$$A_h = \frac{1}{(\Delta x)^2} \begin{pmatrix} -2 & 1 & 0 & \cdots & 0 \\ 1 & -2 & 1 & \cdots & 0 \\ 0 & 1 & -2 & \cdots & 0 \\ \vdots & \vdots & \vdots & \ddots & 1 \\ 0 & 0 & 0 & 1 & -2 \end{pmatrix}. \tag{3.4}$$

Here, $U_\eta(\lambda t)$ denotes the vector approximating the delayed spatial profile

$$(u(\eta x_1, \lambda t), u(\eta x_2, \lambda t), \ldots, u(\eta x_{M-1}, \lambda t))^T.$$

The matrix A_h is symmetric negative definite. Its eigenvalues are

$$\Lambda_j(A_h) = -\frac{4}{(\Delta x)^2} \sin^2\left(\frac{j\pi}{2M}\right), \quad j = 1, \ldots, M-1. \tag{3.5}$$

For completeness, this formula follows directly from the discrete sine modes. For $j = 1, \ldots, M-1$, define

$$v_i^{(j)} = \sin\left(\frac{ij\pi}{M}\right), \quad i = 0, \ldots, M,$$

so that $v_0^{(j)} = v_M^{(j)} = 0$. For each interior index i,

$$(A_h v^{(j)})_i = \frac{v_{i-1}^{(j)} - 2v_i^{(j)} + v_{i+1}^{(j)}}{(\Delta x)^2} = \frac{2\cos(j\pi/M) - 2}{(\Delta x)^2} v_i^{(j)}$$
$$= -\frac{4}{(\Delta x)^2} \sin^2\left(\frac{j\pi}{2M}\right) v_i^{(j)}.$$

Thus, $v^{(j)}$ is an eigenvector of A_h with the stated eigenvalue. Since these $M - 1$ discrete sine vectors are linearly independent, they give the complete spectrum of the Dirichlet finite-difference matrix. Consequently, $A_h - \mu I$ is also symmetric negative definite. This property is the discrete analogue of the dissipativity of the continuous operator $A - \mu I$, and it is the reason for treating this part of the equation implicitly.

3.2. Approximation of the proportional delay term

The proportional delay term requires the numerical solution at the off-grid space-time points

$$(\eta x_i, \lambda t_n), \quad i = 1, \ldots, M - 1.$$

These points generally do not coincide with the computational mesh. Background on numerical methods and continuous approximations for delay differential equations is provided in [17–19]. Continuous Runge-Kutta reconstruction and convergence for retarded and neutral delay equations are analyzed in [20, 21]. We therefore approximate the delayed vector by a two-stage interpolation: first in time and then in space.

Let $t_d = \lambda t_n$. At time level t_n, the fully discrete vector $U^n = (U_1^n, \ldots, U_{M-1}^n)^T$ approximates $(u(x_1, t_n), \ldots, u(x_{M-1}, t_n))^T$, and

$$U^0 = (\phi(x_1, 0), \ldots, \phi(x_{M-1}, 0))^T$$

is the initial nodal vector. The auxiliary vector $\widetilde{U}^n$ introduced below is the reconstruction of the numerical profile at the delayed time t_d; it is not a new time-step solution. The vector $\widehat{U}_\eta^n$ then denotes this delayed-time profile evaluated, by spatial interpolation, at the compressed points ηx_i.

We denote by $\mathcal{I}_\eta$ the piecewise-linear spatial interpolation operator that maps a grid vector V, augmented by the homogeneous boundary values, to its values at the compressed points $\{\eta x_i\}_{i=1}^{M-1}$. Thus, $\widehat{U}_\eta^n = \mathcal{I}_\eta \widetilde{U}^n$.

Since $0 < \lambda < 1$, we have $t_d \leq t_n$. Thus, at time level t_n, the values needed to approximate the delayed state have already been computed. If $t_d = 0$, we set

$$\widetilde{U}^n = U^0.$$

Otherwise, choose $k \leq n - 1$ such that

$$t_k \leq t_d \leq t_{k+1} \leq t_n,$$

and define

$$\theta = \frac{t_d - t_k}{\Delta t} \in [0, 1].$$

The delayed-time profile is reconstructed by linear interpolation:

$$\widetilde{U}^n = (1-\theta)U^k + \theta U^{k+1}. \tag{3.6}$$

Componentwise,

$$\widetilde{U}_j^n = (1-\theta)U_j^k + \theta U_j^{k+1}, \quad j = 1, \ldots, M-1.$$

For interpolation purposes, the interior vector is augmented by the boundary values

$$\widetilde{U}_0^n = \widetilde{U}_M^n = 0.$$

We next evaluate the delayed-time profile at the scaled spatial point

$$x_i^\eta = \eta x_i.$$

Choose $j = j(i)$ such that

$$x_j \le x_i^\eta \le x_{j+1},$$

and define

$$\rho_i = \frac{x_i^\eta - x_j}{\Delta x} \in [0, 1].$$

The delayed value at $(\eta x_i, \lambda t_n)$ is then approximated by

$$\widehat{U}_{\eta,i}^n = (1-\rho_i)\widetilde{U}_j^n + \rho_i \widetilde{U}_{j+1}^n, \quad i = 1, \ldots, M-1. \tag{3.7}$$

Thus,

$$\widehat{U}_\eta^n = (\widehat{U}_{\eta,1}^n, \widehat{U}_{\eta,2}^n, \ldots, \widehat{U}_{\eta,M-1}^n)^T \approx U_\eta(\lambda t_n).$$

This explicit interpolation strategy avoids solving an implicit equation involving delayed and spatially scaled values, while still respecting the causal structure of the pantograph delay.

Remark 3.1. *(Order of the time and space interpolations) For the uniform mesh and linear interpolation used here, reversing the order of the two interpolations gives exactly the same delayed value. Indeed, the time-first, space-second construction yields*

$$\begin{aligned}
\widehat{U}_{\eta,i}^n &= (1-\rho_i)[(1-\theta)U_j^k + \theta U_j^{k+1}] + \rho_i[(1-\theta)U_{j+1}^k + \theta U_{j+1}^{k+1}] \\
&= (1-\theta)[(1-\rho_i)U_j^k + \rho_i U_{j+1}^k] + \theta[(1-\rho_i)U_j^{k+1} + \rho_i U_{j+1}^{k+1}].
\end{aligned}$$

The second line is exactly what is obtained by first interpolating in space at t_k and t_{k+1} and then interpolating those two spatial values in time. Therefore, the two orders produce the same tensor-product bilinear interpolant at $(\eta x_i, \lambda t_n)$. We retain the time-first description because it makes the causal use of already computed time levels particularly transparent. This commutativity is specific to the present linear tensor-product interpolation and need not hold for nonlinear, adaptive, or nonseparable reconstructions.

Remark 3.2. *Higher-order deterministic reconstructions may be used for the delay interpolation. However, for the stochastic problem considered here, the multiplicative Brownian term limits the strong temporal order of the Euler-Maruyama approximation to $1/2$ under standard regularity assumptions [22–24]. Therefore, higher-order deterministic dense output may reduce constants, but it does not change the strong order proved below.*

3.3. Semi-implicit Euler-Maruyama scheme for the stochastic problem

We now discretize the spatially semi-discrete stochastic system in time. Let

$$t_n = n\Delta t, \quad n = 0, 1, \ldots, N,$$

and define the Brownian increment

$$\Delta W_n = W(t_{n+1}) - W(t_n) = \sqrt{\Delta t}\, \xi_n, \quad \xi_n \sim \mathcal{N}(0, 1).$$

The random variables $\{\xi_n\}_{n\geq 0}$ are independent. Hence, ΔW_n is independent of $\mathcal{F}_{t_n}$ and satisfies

$$\mathbb{E}[\Delta W_n] = 0, \quad \mathbb{E}[(\Delta W_n)^2] = \Delta t.$$

Starting from the spatially semi-discrete stochastic system, we treat the stiff diffusion-damping operator $A_h - \mu I$ implicitly, while the proportional delay and multiplicative stochastic terms are evaluated explicitly. Thus, backward Euler is applied to the diffusion-damping part, whereas the stochastic contribution is approximated by the Euler-Maruyama increment. The resulting semi-implicit Euler-Maruyama scheme is

$$U^{n+1} = U^n + \Delta t \left[A_h U^{n+1} - \mu U^{n+1} + \nu \widehat{U}^n_\eta \right] + \sigma U^n \Delta W_n. \tag{3.8}$$

Here, $\widehat{U}^n_\eta$ is the approximation of the delayed spatial profile $U_\eta(\lambda t_n)$ obtained by the time-space interpolation described in Subsection 3.2. Since $0 < \lambda < 1$, we have

$$\lambda t_n \leq t_n.$$

Consequently, $\widehat{U}^n_\eta$ is constructed entirely from the already computed values $U^0, \ldots, U^n$. In particular, if $U^0, \ldots, U^n$ are $\mathcal{F}_{t_n}$-measurable, then so is $\widehat{U}^n_\eta$. Therefore, the numerical update is adapted and does not require future values of the stochastic solution.

Introducing

$$B_h = I - \Delta t(A_h - \mu I), \tag{3.9}$$

the scheme can equivalently be written as

$$B_h U^{n+1} = U^n + \Delta t\, \nu \widehat{U}^n_\eta + \sigma U^n \Delta W_n. \tag{3.10}$$

Thus, at each time level, one generates the scalar Brownian increment ΔW_n, evaluates the delayed profile $\widehat{U}^n_\eta$, forms the random righthand side

$$U^n + \Delta t\, \nu \widehat{U}^n_\eta + \sigma U^n \Delta W_n,$$

and solves a deterministic linear system with coefficient matrix B_h. The randomness of the numerical solution therefore enters through the Brownian increments and the previously computed random states, whereas the implicit solve itself involves the same deterministic matrix at every time step. For fixed Δt and spatial mesh, B_h is independent of n and of the Brownian realization, so its matrix factorization can be computed once and reused throughout the simulation.

The scalar increment ΔW_n acts simultaneously on all spatial components of U^n, consistently with the spatially coherent scalar Brownian forcing in the continuous model. The implicit treatment of $A_h - \mu I$ damps the stiff high-frequency modes generated by the discrete Laplacian, while the explicit treatment of the proportional delay preserves its causal structure. This splitting therefore controls parabolic stiffness without introducing a nonlinear, stochastic, or history-dependent implicit solve.

Lemma 3.1. *(Solvability and discrete damping) For every $\Delta t > 0$, the matrix*

$$B_h = I - \Delta t(A_h - \mu I)$$

is symmetric positive definite. Hence, the linear system defining U^{n+1} has a unique solution at every time step. Moreover,

$$\|B_h^{-1}\|_2 \le \frac{1}{1 + \Delta t(\kappa_{1,h} + \mu)}, \quad \kappa_{1,h} = \frac{4}{(\Delta x)^2} \sin^2\left(\frac{\pi}{2M}\right).$$

Proof. By the spectral representation of A_h established in Subsection 3.1, the eigenvalues of B_h are

$$1 + \Delta t\left[\frac{4}{(\Delta x)^2} \sin^2\left(\frac{j\pi}{2M}\right) + \mu\right], \quad j = 1, \dots, M - 1.$$

These eigenvalues are strictly positive, so B_h is symmetric positive definite. Its smallest eigenvalue is $1 + \Delta t(\kappa_{1,h} + \mu)$, which yields the stated bound.

3.4. Discrete moment stability

We use the discrete L^2-inner product and norm

$$(V, W)_h = \Delta x \sum_{i=1}^{M-1} V_i W_i, \qquad \|V\|_h^2 = (V, V)_h = \Delta x \sum_{i=1}^{M-1} |V_i|^2, \quad V, W \in \mathbb{R}^{M-1}, \tag{3.11}$$

where $\Delta x = L/M$ is the uniform spatial mesh width introduced in Subsection 3.1. Thus, the factor Δx is the quadrature weight in the discrete approximation of the continuous L^2 inner product and norm. The stability of the full scheme depends not only on the implicit damping generated by $A_h - \mu I$, but also on the stability of the interpolation operator used to evaluate the proportional delay.

Assumption 3.1. *(Interpolation stability and consistency) The time and space interpolation operators used to define $\widehat{U}_\eta^n$ satisfy the stability estimate*

$$\mathbb{E}\|\widehat{U}_\eta^n\|_h^2 \le C_\eta \max_{0\le k\le n} \mathbb{E}\|U^k\|_h^2, \quad n \ge 0,$$

where C_η is independent of Δx and Δt. For uniform linear interpolation, $C_\eta \le C\eta^{-1}$, with C independent of Δx and Δt, in agreement with the continuous bound for the spatial pantograph operator.

For the algebraic-decay argument below, we use the corresponding operator-level form of this stability property for the spatial interpolation map $\mathcal{I}_\eta$, namely,

$$\|\mathcal{I}_\eta V\|_h^2 \le C_\eta \|V\|_h^2.$$

For the piecewise-linear spatial reconstruction used in Subsection 3.2 this is the localized version of the same interpolation stability estimate; it allows the two time levels entering $\widetilde{U}^n$ to be retained explicitly.

For the convergence analysis, the interpolation defect in the exact delayed state is assumed to satisfy

$$\left(\mathbb{E}\|\delta_{\mathrm{del}}^n\|_h^2\right)^{1/2} \le C\left((\Delta x)^2 + (\Delta t)^{1/2}\right) + C \max_{0\le k\le n} \left(\mathbb{E}\|e^k\|_h^2\right)^{1/2},$$

where e^k denotes the global error defined in Subsection 3.5.

Remark 3.3. *(Discrete spatial pantograph bound) For piecewise-linear interpolation on a uniform mesh, the discrete delayed profile inherits the qualitative scaling of the continuous operator: $C_\eta \leq C\eta^{-1}$, where C is mesh-independent. Hence, the discrete stability condition contains C_η in the role played by η^{-1} in the continuous estimate.*

To make the stability argument fully explicit, we now retain the exact resolvent factor generated by the implicit diffusion-damping step and expand every term in the conditional second moment. This avoids hiding stability-relevant terms in an unspecified $O((\Delta t)^2)$ remainder and makes the time-step restriction transparent.

Lemma 3.2. *(Exact one-step conditional moment estimate) Let*

$$Y_h^n = \mathbb{E}\|U^n\|_h^2, \quad \gamma_h = \kappa_{1,h} + \mu, \quad r_h = \frac{1}{1 + \gamma_h \Delta t}.$$

Then, the semi-implicit scheme satisfies

$$Y_h^{n+1} \leq r_h^2 \Big[(1 + (\sigma^2 + \nu)\Delta t) Y_h^n + (\nu \Delta t + \nu^2 (\Delta t)^2) \mathbb{E} \|\widehat{U}_\eta^n\|_h^2 \Big]. \tag{3.12}$$

Proof. Because $0 < \lambda < 1$, the delayed value $\widehat{U}_\eta^n$ is constructed from $U^0, \ldots, U^n$ and is therefore $\mathcal{F}_{t_n}$-measurable. The scheme can be written as

$$U^{n+1} = B_h^{-1} R^n, \quad R^n = U^n + \nu \Delta t\, \widehat{U}_\eta^n + \sigma U^n \Delta W_n.$$

Since the discrete L^2-norm differs from the Euclidean norm only by the constant factor Δx, Lemma 3.1 gives

$$\|B_h^{-1} V\|_h \leq r_h \|V\|_h.$$

Conditioning on $\mathcal{F}_{t_n}$ therefore yields

$$\mathbb{E}_n \|U^{n+1}\|_h^2 \leq r_h^2\, \mathbb{E}_n \|R^n\|_h^2, \quad \mathbb{E}_n(\cdot) = \mathbb{E}(\cdot \mid \mathcal{F}_{t_n}).$$

Expanding the square before taking the conditional expectation gives

$$\begin{aligned} \|R^n\|_h^2 &= \|U^n\|_h^2 + 2\nu \Delta t\, (U^n, \widehat{U}_\eta^n)_h + \nu^2 (\Delta t)^2 \|\widehat{U}_\eta^n\|_h^2 \\ &\quad + 2\sigma \Delta W_n \|U^n\|_h^2 + 2\sigma \nu \Delta t\, \Delta W_n (U^n, \widehat{U}_\eta^n)_h + \sigma^2 (\Delta W_n)^2 \|U^n\|_h^2. \end{aligned}$$

The vectors U^n and $\widehat{U}_\eta^n$ are $\mathcal{F}_{t_n}$-measurable, whereas

$$\mathbb{E}_n \Delta W_n = 0, \quad \mathbb{E}_n (\Delta W_n)^2 = \Delta t.$$

Hence, both terms that are linear in ΔW_n vanish after conditioning, and

$$\mathbb{E}_n \|R^n\|_h^2 = (1 + \sigma^2 \Delta t) \|U^n\|_h^2 + 2\nu \Delta t\, (U^n, \widehat{U}_\eta^n)_h + \nu^2 (\Delta t)^2 \|\widehat{U}_\eta^n\|_h^2.$$

Using Young's inequality in the form

$$2(U^n, \widehat{U}_\eta^n)_h \leq \|U^n\|_h^2 + \|\widehat{U}_\eta^n\|_h^2,$$

we obtain

$$\mathbb{E}_n \|R^n\|_h^2 \leq (1 + (\sigma^2 + \nu)\Delta t) \|U^n\|_h^2 + (\nu \Delta t + \nu^2 (\Delta t)^2) \|\widehat{U}_\eta^n\|_h^2.$$

Taking expectations gives (3.12).

Theorem 3.1. *(Discrete mean-square boundedness) Assume Assumption 3.1 and define*

$$\delta_h := 2\kappa_{1,h} + 2\mu - \sigma^2 - \nu(1 + C_\eta).$$

Suppose that $\delta_h > 0$. Set $\gamma_h = \kappa_{1,h} + \mu$. Then, the numerical solution is mean-square bounded for all time levels provided $\Delta t > 0$ is chosen so that

$$\delta_h + (\gamma_h^2 - \nu^2 C_\eta)\Delta t \geq 0. \tag{3.13}$$

In particular, condition (3.13) *holds for every $\Delta t > 0$ if $\gamma_h^2 \geq \nu^2 C_\eta$; if $\gamma_h^2 < \nu^2 C_\eta$, it is sufficient to require*

$$0 < \Delta t \leq \frac{\delta_h}{\nu^2 C_\eta - \gamma_h^2}.$$

Under these conditions,

$$\sup_{n\geq 0} \mathbb{E}\|U^n\|_h^2 \leq \mathbb{E}\|U^0\|_h^2. \tag{3.14}$$

Proof. Let

$$M_h^n = \max_{0\leq k\leq n} Y_h^k, \quad Y_h^k = \mathbb{E}\|U^k\|_h^2.$$

Combining Lemma 3.2 with Assumption 3.1 gives

$$Y_h^{n+1} \leq r_h^2\Big[(1 + (\sigma^2 + \nu)\Delta t)Y_h^n + (\nu\Delta t + \nu^2(\Delta t)^2)C_\eta M_h^n\Big] \leq Q_h(\Delta t)M_h^n,$$

where

$$Q_h(\Delta t) = \frac{1 + [\sigma^2 + \nu(1 + C_\eta)]\Delta t + \nu^2 C_\eta(\Delta t)^2}{(1 + \gamma_h\Delta t)^2}.$$

The stability requirement is therefore $Q_h(\Delta t) \leq 1$. Subtracting the numerator of Q_h from its denominator gives

$$\begin{aligned}(1 + \gamma_h\Delta t)^2 - \Big(1 + [\sigma^2 + \nu(1 + C_\eta)]\Delta t + \nu^2 C_\eta(\Delta t)^2\Big) &= \delta_h\Delta t + (\gamma_h^2 - \nu^2 C_\eta)(\Delta t)^2 \\ &= \Delta t\Big[\delta_h + (\gamma_h^2 - \nu^2 C_\eta)\Delta t\Big].\end{aligned}$$

Thus, (3.13) is exactly the condition ensuring $Q_h(\Delta t) \leq 1$. Consequently,

$$Y_h^{n+1} \leq M_h^n, \quad M_h^{n+1} = \max\{M_h^n, Y_h^{n+1}\} = M_h^n.$$

Induction gives $M_h^n = M_h^0 = Y_h^0$ for every $n \geq 0$, which proves (3.14). The explicit alternatives for Δt follow immediately from the sign of $\gamma_h^2 - \nu^2 C_\eta$.

Remark 3.4. *(Relation with the continuous stability condition) The leading-order discrete stability margin is*

$$\delta_h = 2\kappa_{1,h} + 2\mu - \sigma^2 - \nu(1 + C_\eta).$$

As $\Delta x \to 0$, $\kappa_{1,h} \to (\pi/L)^2$, while the linear interpolation bound has $C_\eta = O(\eta^{-1})$. Thus, the discrete criterion reproduces the same balance between diffusion-damping and noise-delay effects as the continuous energy estimate. The additional condition (3.13) *is the finite-step correction generated by the explicit treatment of the delayed feedback and disappears at leading order as $\Delta t \to 0$.*

The preceding theorem establishes global boundedness. We now show that the same pantograph mechanism also yields an algebraic decay law for the numerical solution. The only additional ingredient is a localized version of the delay interpolation bound, which retains the two time levels that actually enter the linear reconstruction instead of replacing them by a maximum over the whole past history.

Lemma 3.3. *(Localized delayed-profile estimate) For the linear time-space interpolation of Subsection 3.2, let $t_k \le \lambda t_n \le t_{k+1}$ and $\theta_n = (\lambda t_n - t_k)/\Delta t$. Then, for $n \ge 1$,*

$$\mathbb{E}\|\widehat{U}_\eta^n\|_h^2 \le C_\eta\Big[(1-\theta_n)Y_h^k + \theta_n Y_h^{k+1}\Big], \quad Y_h^j = \mathbb{E}\|U^j\|_h^2. \tag{3.15}$$

For $n = 0$, the corresponding estimate is $\mathbb{E}\|\widehat{U}_\eta^0\|_h^2 \le C_\eta Y_h^0$.

Proof. By construction,

$$\widetilde{U}^n = (1-\theta_n)U^k + \theta_n U^{k+1}.$$

Convexity of the squared discrete norm gives

$$\|\widetilde{U}^n\|_h^2 \le (1-\theta_n)\|U^k\|_h^2 + \theta_n\|U^{k+1}\|_h^2.$$

The spatial interpolation at the compressed points ηx_i satisfies the same mesh-independent stability bound used in Assumption 3.1, namely, $\|\widehat{U}_\eta^n\|_h^2 \le C_\eta\|\widetilde{U}^n\|_h^2$. Taking expectations proves (3.15). When $n = 0$, the delayed time is zero and $\widetilde{U}^0 = U^0$, which gives the stated initial estimate.

Theorem 3.2. *(Discrete algebraic mean-square decay) Let Assumption 3.1 hold and use the linear interpolation described in Subsection 3.2. Set*

$$\gamma_h = \kappa_{1,h} + \mu, \quad \alpha_h = 2\gamma_h - \sigma^2 - \nu, \quad \beta_h = \nu C_\eta.$$

Let $q > 0$ be such that

$$\delta_{h,q} + (\gamma_h^2 - \nu\beta_h\lambda^{-q})\Delta t > 0, \quad \delta_{h,q} := \alpha_h - \beta_h\lambda^{-q} > 0. \tag{3.16}$$

Then, there exists a constant $C_{q,h} > 0$ such that

$$\mathbb{E}\|U^n\|_h^2 \le C_{q,h}(1+t_n)^{-q}, \quad n \ge 0. \tag{3.17}$$

Consequently, the zero solution of the fully discrete scheme is mean-square asymptotically stable.

If $\beta_h > 0$, the leading-order part of (3.16) *is*

$$\beta_h\lambda^{-q} < \alpha_h, \quad \textit{equivalently} \quad 0 < q < \frac{\log(\alpha_h/\beta_h)}{\log(1/\lambda)},$$

which is the direct discrete analogue of the exponent restriction in Theorem 2.3. If $\beta_h = 0$, any fixed $q > 0$ is admissible, subject only to the finite-step inequality in (3.16).

Proof. Define

$$R_{h,q} := \frac{1 + [\sigma^2 + \nu + \beta_h \lambda^{-q}]\Delta t + \nu\beta_h\lambda^{-q}(\Delta t)^2}{(1 + \gamma_h \Delta t)^2}.$$

Condition (3.16) is exactly the statement that $R_{h,q} < 1$, because

$$(1 + \gamma_h\Delta t)^2 - \Big(1 + [\sigma^2 + \nu + \beta_h\lambda^{-q}]\Delta t + \nu\beta_h\lambda^{-q}(\Delta t)^2\Big) = \Delta t\Big[\delta_{h,q} + (\gamma_h^2 - \nu\beta_h\lambda^{-q})\Delta t\Big] > 0.$$

Since $R_{h,q} < 1$, we choose the comparison parameter a so that two requirements used in the induction argument hold simultaneously. The first inequality below guarantees that the delayed grid point can be compared with the algebraic envelope at λt_n. The second inequality is chosen so that the one-step amplification factor $R_{h,q}$ does not exceed the decay ratio of the comparison sequence $Z_n = K(a + t_n)^{-q}$; this is precisely what allows $Y_h^{n+1} \le R_{h,q} Z_n$ to imply $Y_h^{n+1} \le Z_{n+1}$. Choose $a \ge 1$ sufficiently large that

$$a(1 - \lambda) \ge \Delta t, \quad R_{h,q} \le \left(\frac{a}{a + \Delta t}\right)^q. \tag{3.18}$$

Such a choice is possible because $R_{h,q} < 1$ and $(a/(a + \Delta t))^q \uparrow 1$ as $a \to \infty$. Set

$$Z_n = K(a + t_n)^{-q},$$

where $K > 0$ is chosen so that $Y_h^0 \le Z_0$.

We prove by induction that $Y_h^n \le Z_n$ for every n. Suppose this is true through level n. For $n \ge 1$, let k be the index used in the delayed-time interpolation, so that $t_k \le \lambda t_n \le t_{k+1}$ and hence $t_k \ge \lambda t_n - \Delta t$. The first condition in (3.18) gives

$$a + t_k \ge a + \lambda t_n - \Delta t \ge \lambda(a + t_n).$$

Since Z_j is decreasing in j, Lemma 3.3 and the induction hypothesis imply

$$\mathbb{E}\|\widehat{U}_\eta^n\|_h^2 \le C_\eta[(1 - \theta_n)Z_k + \theta_n Z_{k+1}] \le C_\eta Z_k \le C_\eta \lambda^{-q} Z_n.$$

The same final bound also holds when $n = 0$, because $\lambda^{-q} \ge 1$ and $\mathbb{E}\|\widehat{U}_\eta^0\|_h^2 \le C_\eta Z_0$.

Applying Lemma 3.2 therefore yields

$$Y_h^{n+1} \le \frac{1 + [\sigma^2 + \nu]\Delta t + C_\eta\lambda^{-q}[\nu\Delta t + \nu^2(\Delta t)^2]}{(1 + \gamma_h\Delta t)^2} Z_n = R_{h,q} Z_n.$$

Moreover,

$$\frac{Z_{n+1}}{Z_n} = \left(\frac{a + t_n}{a + t_n + \Delta t}\right)^q \ge \left(\frac{a}{a + \Delta t}\right)^q \ge R_{h,q}.$$

Thus, $Y_h^{n+1} \le Z_{n+1}$, completing the induction. Finally, $(a + t_n)^{-q} \le C(1 + t_n)^{-q}$, so (3.17) follows.

Remark 3.5. *(Comparison with the analytical decay result) Theorem 3.2 provides the discrete counterpart of Theorem 2.3. In the continuous problem, algebraic decay is governed by $\beta\lambda^{-q} < \alpha$, whereas the discrete scheme requires $\beta_h\lambda^{-q} < \alpha_h$, together with the finite-step correction in* (3.16)*. Thus, as $\Delta t, \Delta x \to 0$, the discrete decay criterion recovers the same pantograph structure as the continuous one.*

3.5. Root mean-square strong convergence

Let $\Pi_h u(t_n)$ denote the nodal projection of the exact solution onto the spatial grid and define the global error

$$e^n = \Pi_h u(t_n) - U^n.$$

The error has three sources: the spatial truncation error of the central difference approximation, the temporal error of the Euler-Maruyama method, and the interpolation error in the proportional delay term.

Theorem 3.3. *(Root mean-square strong convergence) Assume that the exact solution has sufficient spatial and temporal mean-square regularity, for example,*

$$u \in L^2\left(\Omega; C([0,T]; H^4(0,L) \cap H_0^1(0,L))\right),$$

and satisfies the temporal regularity required for the Euler-Maruyama method. Assume also Assumption 3.1 and the discrete stability margin

$$2\kappa_{1,h} + 2\mu - \sigma^2 - \nu(1 + C_\eta) > 0.$$

Suppose that the numerical solution and the projected exact solution are driven by the same Brownian path. Then, for $0 < \Delta t \leq \Delta t_0$,

$$\max_{0 \leq n \leq N} \left(\mathbb{E}\|e^n\|_h^2\right)^{1/2} \leq C_T\left((\Delta x)^2 + (\Delta t)^{1/2}\right),$$

where C_T is independent of Δx and Δt for $0 \leq t_n \leq T$.

Proof. Inserting the projected exact solution into the numerical scheme and subtracting the fully discrete approximation gives the error equation

$$B_h e^{n+1} = e^n + \Delta t\, \nu \delta_{\mathrm{del}}^n + \Delta t\, \tau_x^n + \tau_t^n + \sigma e^n \Delta W_n.$$

Here, τ_x^n is the spatial truncation error, τ_t^n is the Euler-Maruyama temporal defect, and δ_{del}^n is the error associated with the interpolation of the proportional delay term.

The assumed spatial regularity gives

$$\left(\mathbb{E}\|\tau_x^n\|_h^2\right)^{1/2} \leq C(\Delta x)^2.$$

The standard strong local error estimate for Euler-Maruyama gives an accumulated temporal contribution of order $(\Delta t)^{1/2}$. Using Lemma 3.1, conditioning with respect to $\mathcal{F}_{t_n}$, and applying Assumption 3.1, we obtain

$$\mathbb{E}\|e^{n+1}\|_h^2 \leq (1 + C\Delta t) \max_{0 \leq k \leq n} \mathbb{E}\|e^k\|_h^2 + C\Delta t\left((\Delta x)^4 + \Delta t\right).$$

A discrete Gronwall argument yields

$$\max_{0 \leq n \leq N} \mathbb{E}\|e^n\|_h^2 \leq C_T\left((\Delta x)^4 + \Delta t\right).$$

Taking square roots gives

$$\max_{0 \leq n \leq N} \left(\mathbb{E}\|e^n\|_h^2\right)^{1/2} \leq C_T\left((\Delta x)^2 + (\Delta t)^{1/2}\right).$$

Remark 3.6. *The convergence result relies on the stated regularity and interpolation assumptions. The rate $O((\Delta x)^2)$ comes from the central difference approximation, while $O((\Delta t)^{1/2})$ is the classical strong temporal order of Euler-Maruyama for multiplicative noise.*

Remark 3.7. *The parameters η and λ influence stability in different ways. A smaller η increases the spatial-compression effect and therefore reduces the sufficient mean-square stability margin. By contrast, λ does not enter the basic boundedness condition directly, but it affects the admissible algebraic decay rate. Under the stated assumptions, neither parameter changes the theoretical strong convergence order, although both may influence stability bounds and error constants.*

As a result, the semi-implicit Euler-Maruyama method manages stiffness through implicit diffusion-damping, keeps the delay treatment explicit and simple, and preserves the stability and root mean-square convergence properties predicted by the analysis.

4. Numerical simulations

The numerical experiments are designed to support the analytical results developed in Sections 2 and 3, without duplicating tests that convey the same information. We use the stability margin

$$S := 2\left(\frac{\pi}{L}\right)^2 + 2\mu - \sigma^2 - \nu\left(1 + \frac{1}{\eta}\right). \tag{4.1}$$

When $S > 0$, Theorem 2.2 guarantees mean-square boundedness. The tests below examine five aspects: interpolation of the proportional delay, stiffness control of the semi-implicit update, second-order spatial accuracy, root mean-square strong convergence, and the effect of the spatial-scaling parameter η.

All graphical data are generated numerically from the stated models and test problems. Deterministic curves use refined numerical solutions, while stochastic results use simulated Brownian increments and Monte Carlo paths.

All stochastic simulations use

$$\Delta W_n = \sqrt{\Delta t}\,\xi_n, \quad \xi_n \sim N(0, 1).$$

We generate individual sample paths using the semi-implicit Euler-Maruyama scheme. Monte Carlo averages over N_s sample paths are then used to approximate ensemble quantities such as mean-square energy and root mean-square error. Mean-square energy estimates are based on independent Brownian paths, while convergence tests isolate the discretization error. Accordingly, the stability inequalities can be used as conservative pre-simulation screening rules: they indicate parameter regimes in which mean-square boundedness is certified and, in the fully discrete problem, whether an additional time-step restriction is required.

The numerical settings for these five tests are summarized in Table 1.

Table 1. Summary of numerical tests.

Test	Aim	Setup	Paths
1	delay interpolation	$T = 10$, varying Δt	–
2	stiffness control	$T = 2$, $\Delta t = 10^{-4}$–10^{-2}	–
3	spatial accuracy	$T = 5$, $M = 50$–400	–
4	stochastic accuracy	$T = 5$, $M = 200$	500
5	η-sensitivity	$T = 8$, $M = 128$	300

4.1. Delay interpolation check

We first test the interpolation used at off-grid proportional-delay points. Consider the scalar pantograph equation

$$y'(t) = \frac{1}{2}y(t) + \frac{1}{2}e^{t/2}y(\lambda t), \quad y(0) = 1, \tag{4.2}$$

with $\lambda = 0.5$. Its exact solution is $y(t) = e^t$. This test isolates the deterministic time interpolation in the proportional-delay argument.

Figure 2 reports the maximum absolute error as the time step is refined. The nearly straight log-log curve and slope close to one show that the linear reconstruction of $y(\lambda t)$ behaves as expected; this supports the same causal interpolation idea used later in the stochastic partial differential equation (SPDE) scheme.

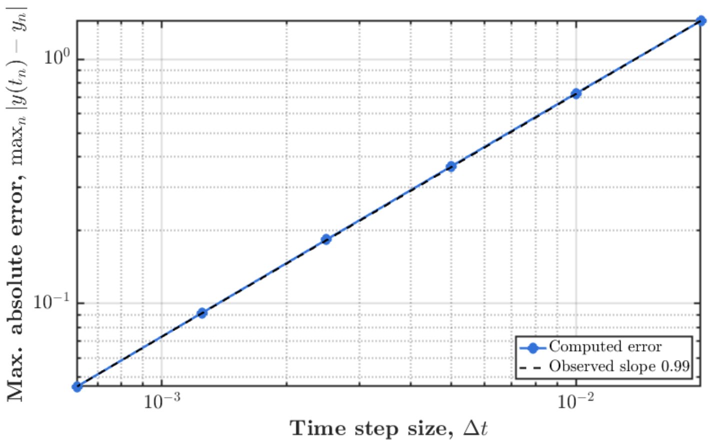

Figure 2. Temporal convergence for the scalar pantograph test (4.2). The observed first-order behavior confirms the accuracy of the interpolation used to evaluate the proportional delay.

4.2. Stiffness control

The next test demonstrates why the parabolic and damping terms are treated implicitly. We consider the stiff scalar pantograph equation

$$y'(t) = -40y(t) + 20y(\lambda t), \quad y(0) = 1, \tag{4.3}$$

with $\lambda = 0.7$. The coefficient -40 produces a fast stable transient. In the semi-implicit update this contribution is damped by a factor of the form $(1 + 40\Delta t)^{-1}$, while a fully explicit update must resolve the stiffness directly.

Figure 3 compares both updates with a fine-step deterministic reference. The semi-implicit curve follows the rapid decay more robustly, supporting the choice in Section 3 to damp the stiff current-state part implicitly while keeping the delayed term explicit.

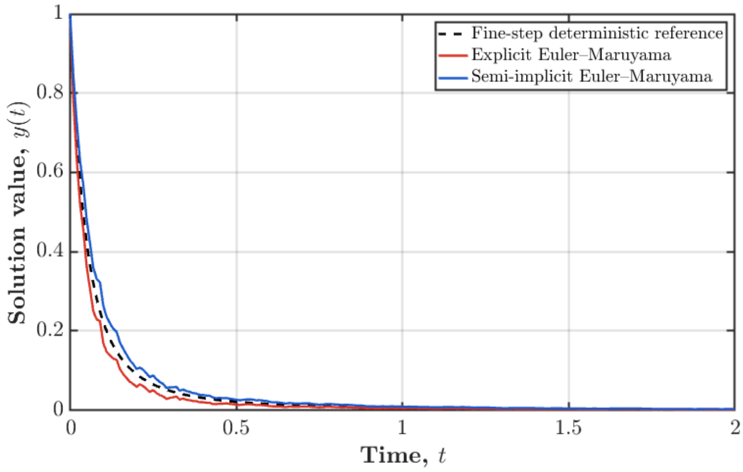

Figure 3. Explicit and semi-implicit updates for the stiff pantograph test. The semi-implicit method is more robust for larger time steps because the stiff current-state damping is treated implicitly.

4.3. Spatial accuracy for the deterministic partial differential equation (PDE)

We next consider the deterministic space-time delayed heat equation

$$\frac{\partial u}{\partial t}(x,t) = \frac{\partial^2 u}{\partial x^2}(x,t) - \mu u(x,t) + \nu u(\eta x, \lambda t), \quad (x,t) \in (0,4) \times (0,T], \tag{4.4}$$

with homogeneous Dirichlet boundary conditions and

$$u(x,t) = \sin(\pi x/4), \quad t \le 0.$$

The parameters are $\mu = 1.5,\ \nu = 0.55,\ \eta = 0.75,\ \lambda = 0.70$. This test isolates the spatial finite-difference error and the interpolation error in the proportional space-time delay.

Figure 4 shows the maximum discrete L^2 error under spatial refinement. The slope close to two confirms the expected second-order spatial behavior and is consistent with the spatial component of the convergence estimate in Theorem 3.3; it also indicates that interpolation at the compressed point ηx does not degrade the observed spatial accuracy.

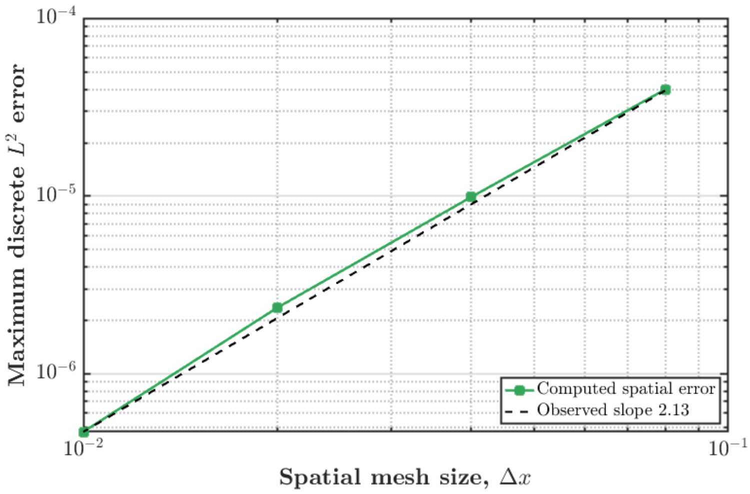

Figure 4. Spatial convergence for (4.4) against a fine-grid reference solution. The observed slope is consistent with second-order central differences and stable delay interpolation.

4.4. Stochastic PDE stability and strong convergence

The main stochastic PDE experiment uses

$$du(x,t) = \left[u_{xx}(x,t) - \mu u(x,t) + \nu u(\eta x, \lambda t)\right] dt + \sigma u(x,t) dW(t), \tag{4.5}$$

with

$$u(0,t) = u(4,t) = 0, \quad u(x,t) = \sin(\pi x/4), \quad t \le 0.$$

Unless otherwise stated, we take $\mu = 2.0$, $\nu = 0.50$, $\eta = 0.80$, $\lambda = 0.70$, $\sigma = 0.30$. For these parameters, $S > 0$; therefore, Theorem 2.2 guarantees mean-square boundedness, while Theorem 2.3 yields algebraic mean-square decay for admissible values of q. The Monte Carlo mean-square energy is computed as

$$E_h^n = \frac{1}{N_s} \sum_{m=1}^{N_s} \|U^{n,m}\|_h^2, \qquad \overline{E}_h^n := \frac{E_h^n}{E_h^0},$$

where $\overline{E}_h^n$ is the normalized mean-square energy plotted below. For convergence tests, the root mean-square strong error is measured against a refined reference solution using common Brownian paths:

$$E_{\Delta x,\Delta t} = \max_{0\le n\le N} \left(\frac{1}{N_s} \sum_{m=1}^{N_s} \|U_{h,\Delta t}^{n,m} - U_{\mathrm{ref}}^{n,m}\|_h^2 \right)^{1/2}.$$

Figure 5 illustrates the stochastic PDE in the stable regime. For the chosen parameters, the normalized mean-square energy remains bounded and exhibits a decreasing trend consistent with the algebraic decay predicted by Theorem 2.3.

Figure 6 complements Figure 5 by assessing strong temporal convergence against a refined reference solution. The root mean-square error decreases under time-step refinement at a rate consistent with the one-half temporal order of Theorem 3.3. Common Brownian paths are used to isolate the discretization error.

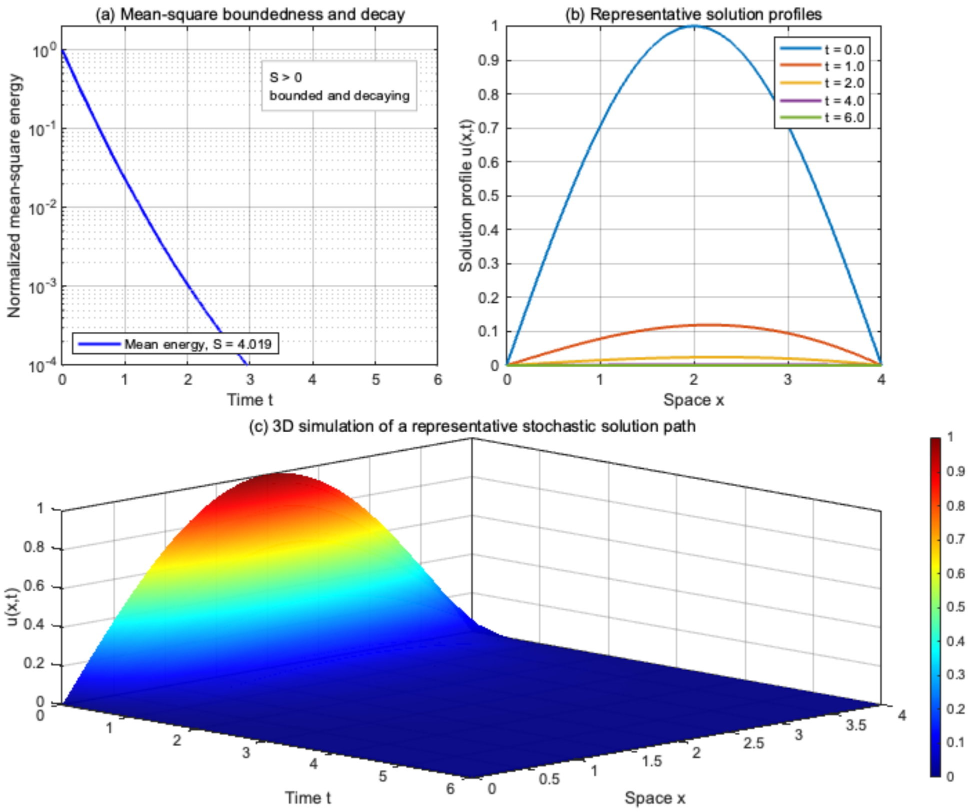

Figure 5. Numerical simulation of the stochastic pantograph heat equation. (a) Normalized mean-square energy demonstrating boundedness and decay. (b) Representative spatial profiles at selected times. (c) Three-dimensional representation of a sample stochastic solution path $u(x, t)$.

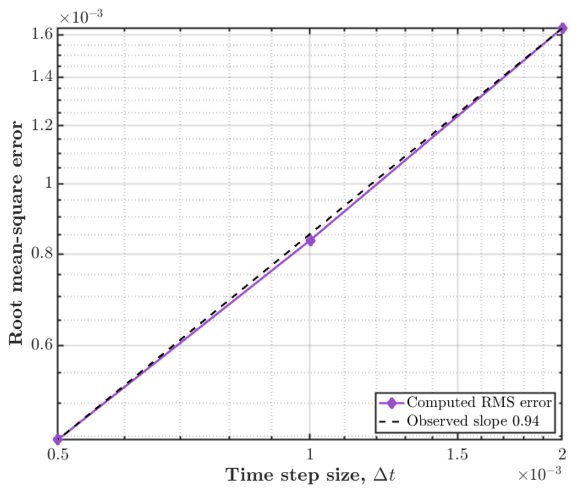

Figure 6. Root mean-square strong convergence of the semi-implicit Euler-Maruyama method. The observed rate is compared with the theoretical temporal order $1/2$ from Theorem 3.3.

4.5. Effect of the spatial scaling parameter η

The final experiment examines the effect of the spatial pantograph scaling parameter η in the stochastic heat equation (4.5). We fix

$$L = 10, \quad \mu = 0.60, \quad \nu = 0.50, \quad \lambda = 0.70, \quad \sigma = 0.30,$$

and vary only η. For this experiment, we use $\Delta t = 0.01$, $M = 128$ spatial subintervals, and $N_s = 300$ independent Monte Carlo sample paths, with initial profile

$$u(x,t) = \sin\left(\frac{\pi x}{L}\right), \quad t \leq 0.$$

To compare the numerical behavior with the analytical stability condition, we consider the sufficient stability margin

$$S(\eta) = 2\left(\frac{\pi}{L}\right)^2 + 2\mu - \sigma^2 - \nu\left(1 + \frac{1}{\eta}\right). \tag{4.6}$$

According to Theorem 2.2, $S(\eta) > 0$ guarantees mean-square boundedness. The critical value defined by $S(\eta_c) = 0$ is

$$\eta_c = \frac{\nu}{2(\pi/L)^2 + 2\mu - \sigma^2 - \nu} \approx 0.619.$$

Thus, for the present parameter set, the sufficient condition guarantees mean-square boundedness when $\eta > \eta_c$, whereas for $\eta \leq \eta_c$ it is inconclusive.

To illustrate the effect of the spatial-scaling parameter, we consider $\eta = 0.95,\ 0.80,\ 0.60,\ 0.40$, which span both regions of the sufficient criterion. The corresponding stability margins are

$$S(0.95) \approx 0.281, \quad S(0.80) \approx 0.182, \quad S(0.60) \approx -0.026, \quad S(0.40) \approx -0.443.$$

Hence, boundedness is guaranteed by Theorem 2.2 for $\eta = 0.95$ and $\eta = 0.80$, while no stability conclusion follows from this sufficient criterion for $\eta = 0.60$ and $\eta = 0.40$. In particular, a negative value of $S(\eta)$ should not be interpreted as evidence of instability.

Figure 7 compares the numerical mean-square energy with the theoretical stability margin. Panel (a) shows the normalized Monte Carlo energy, while panel (b) shows the corresponding values of $S(\eta)$. As η decreases, the η^{-1} spatial-scaling penalty increases, reducing the stability margin. Since $S(\eta) > 0$ is only a sufficient condition, the trajectories need not be monotone in η; thus, decay observed for $S(\eta) \leq 0$ does not contradict the theory, but rather reflects the conservativeness of the criterion.

The η-sensitivity experiment illustrates a practical use of the theory. For fixed domain length, damping, feedback strength, and noise intensity, the stability condition gives a critical spatial-scaling value before Monte Carlo simulation. Here, $\eta_c \approx 0.619$, so $\eta = 0.95$ and 0.80 lie in the guaranteed stable region, whereas $\eta = 0.60$ and 0.40 require numerical assessment. Since the condition is only sufficient, failure of the inequality does not imply instability. Together with the discrete step-size condition, this provides a simple screening tool for stability and discretization effects.

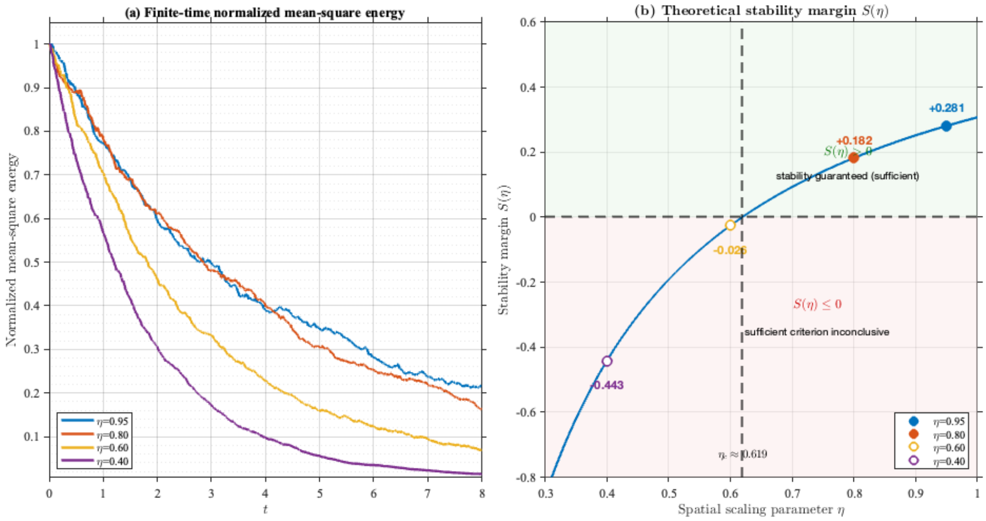

Figure 7. Effect of the spatial scaling parameter η. (a) Finite-time normalized mean-square energy for selected values of η. (b) Theoretical stability margin $S(\eta)$. The dashed lines indicate $S(\eta) = 0$ and the critical value $\eta_c \approx 0.619$. For $\eta > \eta_c$, mean-square boundedness is guaranteed by the sufficient criterion; for $\eta \leq \eta_c$, the criterion is inconclusive.

5. Conclusions

We studied a stochastic heat equation with proportional space-time delay $u(\eta x, \lambda t)$ and multiplicative Brownian noise. The key analytical feature is the spatial pantograph operator $(Pv)(x) = v(\eta x)$, whose bound

$$\|Pv\|^2_{L^2(0,L)} \leq \eta^{-1}\|v\|^2_{L^2(0,L)}$$

introduces the stability penalty η^{-1} associated with spatial compression. This yields the sufficient mean-square stability condition

$$2\left(\frac{\pi}{L}\right)^2 + 2\mu > \sigma^2 + \nu\left(1 + \frac{1}{\eta}\right),$$

under which the second moment is uniformly bounded and decays algebraically. A less conservative weighted condition was also obtained. The parameter λ does not enter the basic boundedness condition directly but influences the admissible algebraic decay rate, while $\eta = 1$ recovers the proportional time-delay setting.

For the numerical approximation, we proposed a semi-implicit finite-difference Euler-Maruyama scheme that treats diffusion and damping implicitly and the delay and stochastic terms explicitly. Under suitable interpolation and step-size conditions, the method preserves mean-square boundedness and algebraic decay and satisfies

$$\max_{0\leq n\leq N}\left(\mathbb{E}\|\Pi_h u(t_n) - U^n\|_h^2\right)^{1/2} \leq C_T\left((\Delta x)^2 + (\Delta t)^{1/2}\right).$$

The numerical experiments support the theoretical stability and convergence results and illustrate the influence of the spatial-scaling parameter η. In particular, stronger spatial compression reduces the sufficient stability margin, consistently with the η^{-1} penalty. Future work will address multidimensional stochastic pantograph equations and more general spatial domains.

Use of Generative-AI tools declaration

The author declares he has not used Artificial Intelligence (AI) tools in the creation of this article.

Conflict of interest

The author declares no conflict of interest.

References

1. J. R. Ockendon, A. B. Tayler, The dynamics of a current collection system for an electric locomotive, *Proc. R. Soc. Lond. Ser. A Math. Phys. Sci.*, **322** (1971), 447–468.
2. A. Iserles, On the generalized pantograph functional-differential equation, *Eur. J. Appl. Math.*, **4** (1993), 1–38. https://doi.org/10.1017/S0956792500000966
3. F. A. Rihan, *Delay differential equations and applications to biology*, 2 Eds., Cham: Springer, 2026. https://doi.org/10.1007/978-3-032-08645-7
4. A. D. Polyanin, V. G. Sorokin, Exact solutions and reductions of nonlinear diffusion PDEs of pantograph type, 2021, arXiv: 2103.01666.
5. F. A. Rihan, A. F. Rihan, An analysis of the theta-method for pantograph-type delay differential equations, *Complexity*, **2022** (2022), 8961352. https://doi.org/10.1155/2022/8961352
6. F. A. Rihan, Continuous Runge-Kutta schemes for pantograph type delay differential equations, *Partial Differ. Equ. Appl. Math.*, **11** (2024), 100797. https://doi.org/10.1016/j.padiff.2024.100797
7. F. A. Rihan, K. Udhayakumar, Split-step θ-method for stochastic pantograph differential equations: convergence and mean-square stability analysis, *Appl. Numer. Math.*, **217** (2025), 1–17. https://doi.org/10.1016/j.apnum.2025.05.010
8. J. Alzabut, A. G. M. Selvam, R. A. El-Nabulsi, D. Dhakshinamoorthy, M. E. Samei, Asymptotic stability of nonlinear discrete fractional pantograph equations with non-local initial conditions, *Symmetry*, **13** (2021), 1–22. https://doi.org/10.3390/sym13030473
9. T. S. Hassan, R. G. Ahmed, A. M. A. El-Sayed, R. A. El-Nabulsi, O. Moaaz, M. B. Mesmouli, Solvability of a state-dependence functional integro-differential inclusion with delay nonlocal condition, *Mathematics*, **10** (2022), 1–18. https://doi.org/10.3390/math10142420
10. S. S. Santra, R. A. El-Nabulsi, K. M. Khedher, Oscillation of second-order differential equations with multiple and mixed delays under a canonical operator, *Mathematics*, **9** (2021), 1–9. https://doi.org/10.3390/math9121323
11. A. Shahid, H. L. Huang, M. M. Bhatti, M. Marin, Numerical computation of magnetized bioconvection nanofluid flow with temperature-dependent viscosity and Arrhenius kinetic, *Math. Comput. Simul.*, **200** (2022), 377–392. https://doi.org/10.1016/j.matcom.2022.04.032
12. S. Askar, A. E. Abouelregal, M. Marin, A. Foul, Photo-thermoelasticity heat transfer modeling with fractional differential actuators for stimulated nano-semiconductor media, *Symmetry*, **15** (2023), 1–18. https://doi.org/10.3390/sym15030656

13. S. E. A. Mohammed, *Stochastic functional differential equations*, Boston: Pitman, 1984.
14. G. Da Prato, J. Zabczyk, *Stochastic equations in infinite dimensions*, Cambridge University Press, 1992.
15. C. Prévôt, M. Röckner, *A concise course on stochastic partial differential equations*, Berlin, Heidelberg: Springer, 2007. https://doi.org/10.1007/978-3-540-70781-3
16. X. R. Mao, *Stochastic differential equations and applications*, 2 Eds., Chichester: Horwood Publishing, 2007.
17. G. A. Bocharov, F. A. Rihan, Numerical modelling in biosciences using delay differential equations, *J. Comput. Appl. Math.*, **125** (2000), 183–199. https://doi.org/10.1016/S0377-0427(00)00468-4
18. A. Bellen, M. Zennaro, *Numerical methods for delay differential equations*, Oxford University Press, 2003.
19. C. T. H. Baker, C. A. H. Paul, D. R. Willé, Issues in the numerical solution of evolutionary delay differential equations, *Adv. Comput. Math.*, **3** (1995), 171–196. https://doi.org/10.1007/BF02988625
20. W. H. Enright, H. Hayashi, A delay differential equation solver based on a continuous Runge-Kutta method with defect control, *Numer. Algorithms*, **16** (1997), 349–364. https://doi.org/10.1023/A:1019107718128
21. W. H. Enright, H. Hayashi, Convergence analysis of the solution of retarded and neutral delay differential equations by continuous numerical methods, *SIAM J. Numer. Anal.*, **35** (1998), 572–585. https://doi.org/10.1137/S0036142996302049
22. P. E. Kloeden, E. Platen, *Numerical solution of stochastic differential equations*, Berlin, Heidelberg: Springer, 1992. https://doi.org/10.1007/978-3-662-12616-5
23. G. N. Milstein, *Numerical integration of stochastic differential equations*, Dordrecht: Springer, 1995.
24. D. J. Higham, An algorithmic introduction to numerical simulation of stochastic differential equations, *SIAM Rev.*, **43** (2001), 525–546. https://doi.org/10.1137/S0036144500378302

AIMS Press